nanomaterials

MDPI

Communication

Defect-Rich Monolayer MoS_2 as a Universally Enhanced Substrate for Surface-Enhanced Raman Scattering

Shiyu Sun [1,†], Jingying Zheng [2,†], Ruihao Sun [1], Dan Wang [1], Guanliang Sun [1], Xingshuang Zhang [1], Hongyu Gong [1], Yong Li [1], Meng Gao [1], Dongwei Li [1,*], Guanchen Xu [1,*] and Xiu Liang [1,*]

[1] Key Laboratory for High Strength Lightweight Metallic Materials of Shandong Province (HM), Advanced Materials Institute, Qilu University of Technology (Shandong Academy of Sciences), Jinan 250014, China; sysun0313@163.com (S.S.); srh1645@163.com (R.S.); Wangdan1910@163.com (D.W.); 13793994223@163.com (G.S.); xszhang@qlu.edu.cn (X.Z.); hygong@sdas.org (H.G.); yongli@sdas.org (Y.L.); mgao@sdas.org (M.G.)

[2] College of Materials Science and Engineering, Fuzhou University, Fuzhou 350108, China; jyzheng@fzu.edu.cn

* Correspondence: dwli@sdas.org (D.L.); gcxu@sdas.org (G.X.); xliang@sdas.org (X.L.)

† These authors contributed equally to this work.

Abstract: Monolayer 2H-MoS_2 has been widely noticed as a typical transition metal dichalcogenides (TMDC) for surface-enhanced Raman scattering (SERS). However, monolayer MoS_2 is limited to a narrow range of applications due to poor detection sensitivity caused by the combination of a lower density of states (DOS) near the Fermi energy level as well as a rich fluorescence background. Here, surfaced S and Mo atomic defects are fabricated on a monolayer MoS_2 with a perfect lattice. Defects exhibit metallic properties. The presence of defects enhances the interaction between MoS_2 and the detection molecule, and it increases the probability of photoinduced charge transfer (PICT), resulting in a significant improvement of Raman enhancement. Defect-containing monolayer MoS_2 enables the fluorescence signal of many dyes to be effectively burst, making the SERS spectrum clearer and making the limits of detection (LODs) below 10^{-8} M. In conclusion, metallic defect-containing monolayer MoS_2 becomes a promising and versatile substrate capable of detecting a wide range of dye molecules due to its abundant DOS and effective PICT resonance. In addition, the synergistic effect of surface defects and of the MoS_2 main body presents a new perspective for plasma-free SERS based on the chemical mechanism (CM), which provides promising theoretical support for other TMDC studies.

Keywords: MoS_2; surface defects; surface-enhanced Raman scattering; photoinduced charge transfer; metallic

Citation: Sun, S.; Zheng, J.; Sun, R.; Wang, D.; Sun, G.; Zhang, X.; Gong, H.; Li, Y.; Gao, M.; Li, D.; et al. Defect-Rich Monolayer MoS_2 as a Universally Enhanced Substrate for Surface-Enhanced Raman Scattering. *Nanomaterials* **2022**, *12*, 896. https://doi.org/10.3390/nano12060896

Academic Editor: Sammy W. Verbruggen

Received: 12 February 2022
Accepted: 4 March 2022
Published: 8 March 2022

1. Introduction

Two-dimensional transition metal dichalcogenides (TMDCs) have been very popular semiconductor materials with potential applications in many fields due to their unique structural and physicochemical properties [1–5]. Typically, semiconductor monolayers of MoS_2 are of great interest for applications in electronic sensor devices, energy storage applications, catalytic fields, and composite materials. Additionally, MoS_2 monolayers are substrates for potential applications of surface-enhanced Raman scattering (SERS) based on molecular detection, which strongly depends on the electronic and optoelectronic properties of monolayer MoS_2 [6]. SERS is a nondestructive and useful quantitative analysis technique that is widely used because of its low cost, ease of synthesis, excellent optical properties, and biocompatibility [7–12]. The core of SERS research is the preparation of substrates [10,13–16], which requires a perfect balance between enhancement capability, homogeneity, stability, and economy. SERS substrate materials are enhanced by different mechanisms, which are the electromagnetic mechanism (EM) and the chemical mechanism (CM) [17–19]. The EM originates from localized surface plasmon resonance generated by

metal nanostructures. The local amplified "hot spot" generated by surface plasmon resonance (SPR) is usually composed of noble metal nanoparticles (Au, Ag, or Cu), which have high SERS activity and detection sensitivity [20–24]. There is no substitute for precious metals, as SERS detection substrates, but they have the disadvantages of high cost and instability. In addition, there are problems of biocompatibility and chemical interactions between the detection molecule and the substrate in the process, and these problems seriously limit the market application of precious metal SERS substrates. The CM is mainly a charge transfer (CT) generated by the interaction between the chemistry of the detection molecule and the substrate. The CM is considered the main enhancement mechanism for 2D materials, such as graphene [25,26] and TMDCs [27,28]. The Raman signal generated by the nonmetallic SERS substrate represented by MoS_2 is a combination of photoinduced charge transfer (PICT) between the dye molecule and the substrate as well as local dipoles resulting from changes in molecular symmetry [29–31]. Such substrates not only have higher SERS homogeneity but also better chemical stability and biocompatibility [32]. In addition to the unique enhancement mechanism, the surface of the 2D material allows for uniform chemisorption of dye molecules, which is essential for reproducible signal collection and practical applications [19,33]. However, the detection performance of monolayer MoS_2 as a SERS substrate is lower than the enhancement brought by noble metals due to its high charge recombination rate, low electrical conductivity, limited catalytic active sites, and weak charge transfer. The precise control and modulation of the electronic and optoelectronic properties of MoS_2 can improve its versatility. According to Fermi's golden rule, the electron leap probability of the SERS process is linearly related to the density of states near the Fermi energy level [9,27,34]. In recent years, many tuning strategies have been applied to increase the density of states (DOS) in the semiconductor bandgap to in turn improve the PICT efficiency [27]. A range of techniques for fabricating defects has been developed, including phase transitions [35], plasma treatment [36], and oxygen doping [32], among others [37]. Notably, these defect-enhanced methods for improving the SERS performance of 2D materials are complex and extremely limited, if not negative. For this reason, it is necessary to develop a simple and widely applicable defect engineering strategy based on monolayer MoS_2 that does not change the overall material properties while achieving high electron density [2,38]. In addition, Warner et al. provided a new idea for surface defects by demonstrating that increasing the width of linear defects leads to reconstructed nanoscale regions of monolayer MoS_2, which density functional theory (DFT) shows to exhibit metallicity [39].

Here, for the first time, we use experiments and theory to investigate the Raman enhancement effect of monolayer MoS_2 before and after the presence of surface defects. In this paper, large-scale, highly crystalline samples were prepared under the precise control of the chemical vapor deposition (CVD) method with sulfur powder and electroplated molybdenum foil as precursors of the monolayer MoS_2 and with SiO_2/Si as substrates [40–42]. Indeed, due to the strong fluorescence background and inefficient CT, it is difficult to visualize the SERS signal in perfect MoS_2 monolayers, especially when the surface contains low concentrations of detected molecules. In contrast, monolayers of MoS_2 containing a small number of defects are produced by short-term, high-temperature etching in a constant low-pressure environment with only a small amount of air. Monolayer MoS_2 containing etched regions exhibits the unique advantage of abundant DOS near the Fermi energy level and more intense CT and PICT efficiency. This strategy is broad, with a wide range of detection molecules being detected and reaching limits of detection (LODs) of less than 10^{-8} M. Theoretical calculations further confirm that monolayer MoS_2 in the etched region possesses a narrower bandgap and exhibits metallic properties. Metallic MoS_2 has abundant DOS near the Fermi energy level and strong interactions with detection molecules, making it ideal as a promising enhanced substrate for SERS applications.

2. Materials and Methods

2.1. Synthesis of Monolayer MoS_2

The monolayer MoS_2 nanosheets are prepared through a CVD system using sulfur and molybdenum sources as precursors. Prepare the electrolyte with Na_2SO_4 (Aladdin Reagents, 99.0%), NaF (Aladdin Reagents, 99.93%), and $H_2C_2O_4$ (Macklin, 99.0%) according to a specific ratio, and perform anodizing at room temperature with a voltage of 0.4~0.6 V and a time of 30 min. In the CVD system, the sulfur powder (Macklin, 99.99%) in the corundum boat is placed upstream of the pipeline, and the electroplated molybdenum foil on the SiO_2/Si wafer is placed in the center of the furnace. A separate heating zone is the heat source for sulfur sublimation. When the heating zone reaches 150 °C, the temperature of the molybdenum source just reaches 850 °C, and all react in the Ar atmosphere for 15 min. When the temperature in the furnace drops to 50 degrees Celsius, the heating of the S source is stopped. Keep the Ar atmosphere until the system reaches room temperature.

2.2. Synthesis of Etched MoS_2

The perfect monolayer MoS_2 is selected to prepare defects to reduce experimental errors. MoS_2 is placed in the center of the furnace with one end sealed, and the other end is a continuously working vacuum oil pump. An etching environment that is almost isolated from the outside world with only a small amount of air is created at a low vacuum of 0.02 Torr. In order to maintain the crystal structure of MoS_2, the etching temperature is controlled below the growth temperature, and the reaction time is within a few minutes.

2.3. Materials Characterization

The morphology of molybdenum foil was characterized by SEM (S4800, Hitachi, Tokyo, Japan). A three-electrode system and a CHI 760D (Shanghai, China) electrochemical workstation were used for the electrochemical experiment. Optical images were captured with an Olympus BX 53 M microscope (Tokyo, Japan). AFM from a Bruker bioscope resolve system and silicon cantilevers from nano sensors were used for intelligent mode operation. Raman spectra were recorded from a Horiba JY iHR550 (Tokyo, Japan) system with an excitation wavelength at 532 nm. During measurements, the laser beam was focused on a spot with a 1 μm diameter by a microscope objective with a magnification of 50×, and the acquisition time was set to 5 s.

2.4. SERS Measurements

Rhodamine 6G (R6G), methylene blue (MB), and crystal violet (CV) dyes were used as Raman probe molecules to first verify the SERS properties of etched MoS_2 substrate. Briefly, 15 μL of R6G, CV, and MB probes with different concentrations (10^{-4}–10^{-9} M) were consecutively dropped on the surface of the etched substrate. The laser power on the sample was 50 mW with a 5 s exposure time under 532 nm laser excitation. We calculated the enhancement factor (EF) values using the following equation:

$$EF = \frac{I_{SERS}/N_{SERS}}{I_{NR}/N_{NR}}$$

where I_{SERS} and I_{NR} refer to the Raman intensity of probe molecules in the SERS and Raman spectra, and N_{SERS} and N_{NR} are the estimated molecule number under laser excitation for SERS and the molecule number for the reference sample (solid), respectively.

2.5. DFT Calculation Details

In the framework of the density functional theory (DFT), the generalized gradient approximation and projector broadening plane wave method proposed by Perdew, Burke, and Ernzerhof was used in the framework of density generalized function theory at a kinetic energy cutoff of 400 eV, as implemented in the Vienna ab initio simulation package (VASP 5.4.4) [43,44]. The Brillouin zone of the surface unit cell was sampled by Monkhorst–Pack (MP) grids, with a different k-point mesh for MoS_2 structure optimizations. The MoS_2

surface was determined by a 2 × 2 × 1 Monkhorst−Pack grid. The convergence criterion for the electronic self-consistent iteration and force was set to 10^{-5} eV and 0.01 eV/Å, respectively. A 6 × 6 supercell of the MoS_2 surface, including one layer, was constructed to model the MoS_2 catalyst in this work. A vacuum layer of 15 Å was introduced to avoid interactions between periodic images.

3. Results and Discussion

Controllable preparation of the material is the key to achieving practical applications of single-molecule thick MoS_2. Figure 1a examines a series of advances centered on monolayer MoS_2, including preparation, evaluation of MoS_2 containing defects, and characterization of various SERS properties. Sublimable sulfur powder and molybdenum foil were used to prepare monolayer MoS_2 in a CVD system, which was an improvement demonstrated in previous works [40,41]. The metallic molybdenum foil was electroplated and treated on an electrochemical workstation. Its activity was enhanced to be more favorable for the reaction (Figure S1). Specifically, the growth process is such that the CVD is designed with two different temperature-controlled zones, and when Mo reaches the MoS_2 growth temperature, the S vapor rapidly fills the entire system (Figure S2). Both vapors collect simultaneously on the SiO_2/Si substrate and rapidly nucleate growth with a size of approximately 30 µm, as shown in Figure 1b,e.

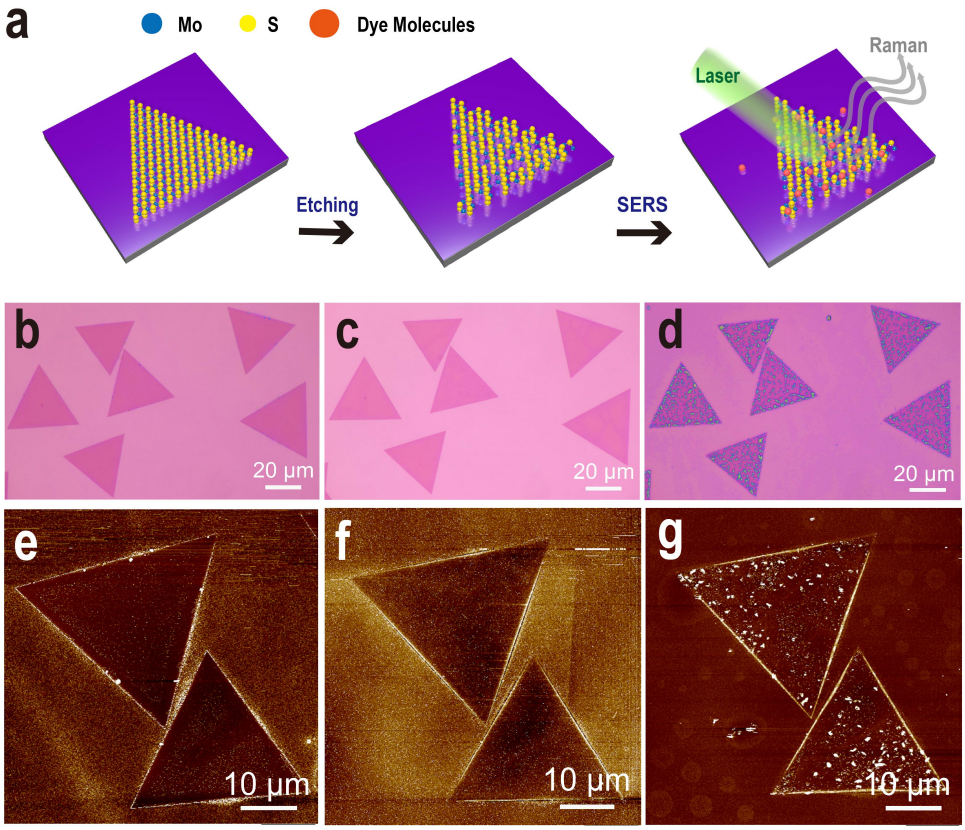

Figure 1. (**a**) Simple schematic illustrating the process of SERS detection after etching monolayer MoS_2 grown on the same SiO_2/Si substrate. Optical microscopy image (**b**–**d**) and AFM image (**e**–**g**) of the monolayer MoS_2, the etched monolayer MoS_2, and the etched monolayer MoS_2 with dye molecules added dropwise.

Here, based on the above monolayer MoS_2, a simple and practical defect preparation strategy is proposed: a thermal etching process in a low-vacuum system. Given the complex variation of external conditions, a vacuum pressure oil pump maintains the internal pressure in a closed environment at a low vacuum of 0.02 Torr and externally applies a high temperature of ~800 °C below the growth temperature (Figure S3), which creatively

generates abundant defects in a short time. The etching conditions were chosen for the case of moderate etching as a result of several experiments (Figure S4). The extended pumping time before etching and the presence of excess S monomer on the SiO_2/Si substrates with a monolayer of MoS_2 serve to minimize the effect of oxidizing gases in the confined system. This approach is very clever, neither destroying the structure of the monolayer MoS_2 nor producing only the absence of Mo and S atoms. These subtle changes are indistinguishable under optical microscopy (Figure 1b,c), but can be observed under atomic force microscopy (AFM), as seen in Figure 1e,f. The etched MoS_2 surface becomes rough and the corresponding impurities on the SiO_2/Si substrate are largely removed (Figure S5a,b). A more objective SERS detection property is that the MoS_2 surface containing defects adsorbs more dye molecules, which is reflected in the optical photographs and AFM in Figure 1d,g. Strong chemisorption enhances the connection between the substrate and the dye molecules, which enhances the CT and coupling effects. Relatively, the monolayer MoS_2 surface adhesion is small and uneven (Figure S6).

MoS_2 underwent a large change during the etching process. The Raman spectrum was obtained using a 532 nm laser line with a spot size of approximately 1 µm. From the Raman spectra in Figure 2a, two characteristic MoS_2 peaks are located at ~383.0 cm^{-1} and ~401.9 cm^{-1}, which are associated with in-plane (E^1_{2g}) and out-of-plane (A_{1g}) vibrational modes, respectively [45]. The peak spacing between the two characteristic peaks is ~19 cm^{-1}, which confirms the monolayer structure of MoS_2. After the appearance of surface defects in the MoS_2, the two Raman characteristic peaks are shifted, and the peak spacing becomes wider. It is worth mentioning that the characteristic peak A_{1g} in the etched MoS_2 Raman spectrum is shifted approximately 1 cm^{-1} in the high wavenumber direction due to a small amount of air remaining in the confined environment reacting with the MoS_2.

The photoluminescence spectra (PL) spectra show that defects can affect the bandgap of the semiconductor and cause fluorescence bursts in MoS_2 (Figure S7). The calculated energy band structure yields a bandgap of approximately 1.70 eV for monolayer MoS_2 (Figure S8), whereas MoS_2 at the defect exhibits strong metallic properties of only 0.07 eV (Figure 2b). X-ray photoelectron spectroscopy (XPS) was used to demonstrate the chemical state of the monolayer MoS_2 after etching, by comparing commercial MoS_2 powder with defect-less monolayer MoS_2. The in situ semi-quantitative analysis by XPS shows that the content of Mo in defect-rich MoS_2 decreases from 2.48% to 1.74% and that S decreases from 3.78% to 2.01% relative to the unetched sample. Both the Mo 3d and S 2p spectra of the MoS_2 can be fitted well, indicating the elemental composition and valence states in Figure 2c,d. The binding energy peaks at 229.6 eV and 232.7 eV for monolayer MoS_2 are caused by Mo^{4+} $3d_{5/2}$ and $3d_{3/2}$. The peak at 233.8 eV corresponds to Mo^{6+} $3d_{5/2}$, and the peak at 235.9 eV corresponds to Mo^{6+} $3d_{3/2}$. The Mo^{6+} is due to a small number of oxidation peaks due to the great difference between the CVD system and the external environment during the preparation process and due to the inverse concentration gradient flow of O_2 in the air. The monolayer MoS_2 is etched at a high temperature and a low air concentration, the Mo 3d XPS spectral peak shifts in the direction of the low binding energy, the Mo^{4+} $3d_{3/2}$ content decreases, and the Mo^{6+} content disappears completely but is replaced by Mo^{5+} $3d_{5/2}$ at 232.7 eV and Mo^{5+} $3d_{3/2}$ at 235.6 eV. The presence of S $2p_{1/2}$ and S $2p_{3/2}$ spin-orbit bimodal peaks in the monolayer MoS_2 is related to Mo-S bonding. Curiously, S^{6+} appears in the MoS_2 monolayer due to the residual SO_4^{2-} ion during the plating of the molybdenum foil used for the preparation of the monolayer MoS_2 precursor by the CVD method. The complete disappearance of S^{6+} after the etching process is one of the reasons why the S 2p XPS spectrum also moves toward low binding energy. Comparing the Mo 3d and S 2p of commercial MoS_2 powders, no significant Mo-O and S-O bonds appear after the etching reaction. The enhancement of SERS performance due to surface defects is mainly due to Mo and S defects rather than O_2. The binding energy of the XPS spectra of O1s etched with MoS_2 did not change compared to that of monolayer MoS_2 (Figure S9). For commercial MoS_2, no Mo-O bond exists before etching, so there is no effect of oxygen defects even after the reaction.

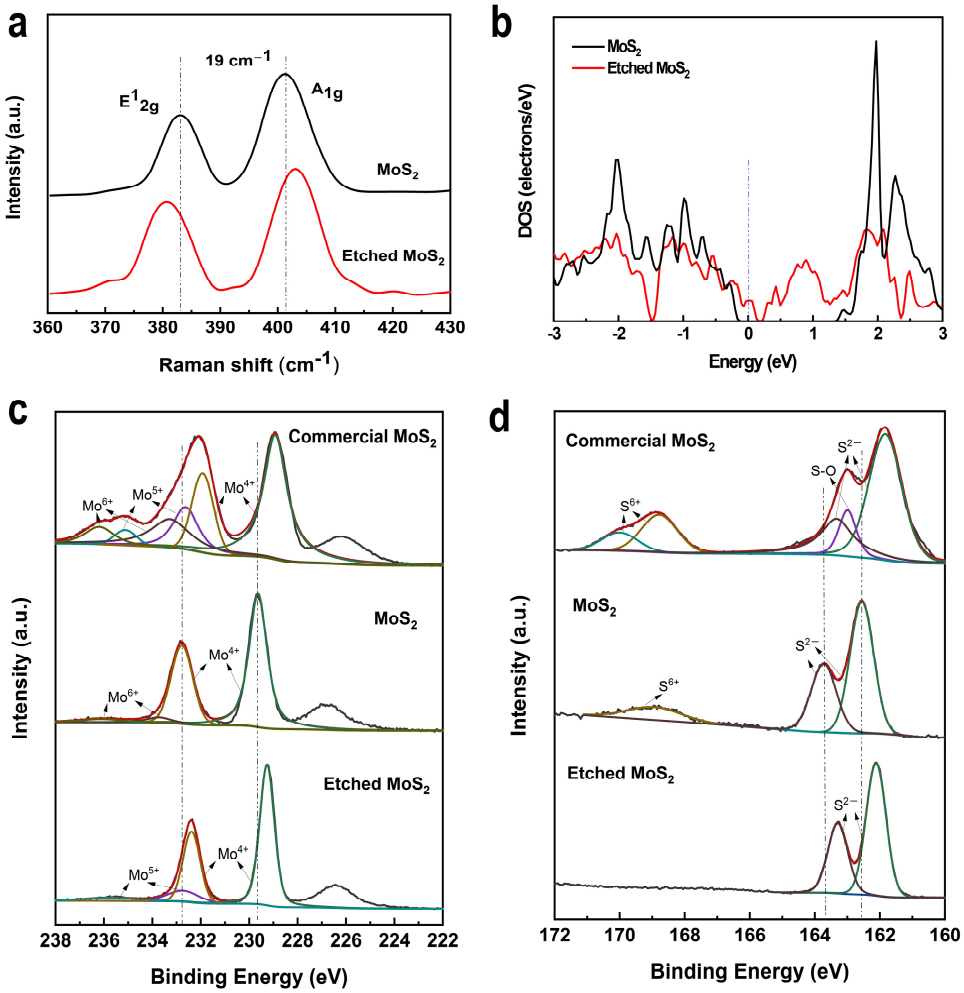

Figure 2. (**a**) Raman spectra and density of states of CVD grown MoS_2 and etched monolayer MoS_2. (**b**) Calculated band structures of etched MoS_2 using the Fermi level as a reference. XPS data of commercial MoS_2 powder, CVD grown monolayer MoS_2, and etched monolayer MoS_2 at the binding energies of (**c**) Mo 3d and (**d**) S 2p.

To investigate the SERS effect of MoS_2 on SiO_2/Si substrates, rhodamine 6G (R6G) was first used as a probe molecule. A series of R6G solutions were prepared from 10^{-8} M to 10^{-4} M to investigate the SERS sensitivity of 2D etched monolayer MoS_2. There was a significant difference in the SERS behavior between monolayer MoS_2 without defects and the etched MoS_2 (Figure 3a). The 10^{-4} M concentration of R6G solution added dropwise to the clean SiO_2/Si substrate did not result in any detectible SERS signal. At the same concentration, the Raman signal of the unetched monolayer MoS_2 grown on SiO_2/Si as a substrate for SERS detection was barely detectable due to the interference of the fluorescence background. Monolayer MoS_2 containing defects exhibited exaggerated SERS performance. The characteristic R6G peaks located at 611, 773, 1360, and 1640 cm^{-1}, could be easily observed on the etched MoS_2, which were assigned to the C−H ring in-plane bending of the xanthenes skeleton, C−H out-of-plane bending, CH_3 bending, and C–C stretching vibration modes, respectively [9,30]. The chemisorption caused a certain degree of distortion and polarization of the molecular structure, which shifted the vibrational band compared to the normal Raman spectrum of the R6G powder. When the concentration of R6G reached 10^{-8} M, it was still detectable that the monolayer MoS_2 substrates contain defects. The data show an enhancement factor (EF) of 10^5, which is comparable to that of noble metal-based SERS substrates (Figure S10).

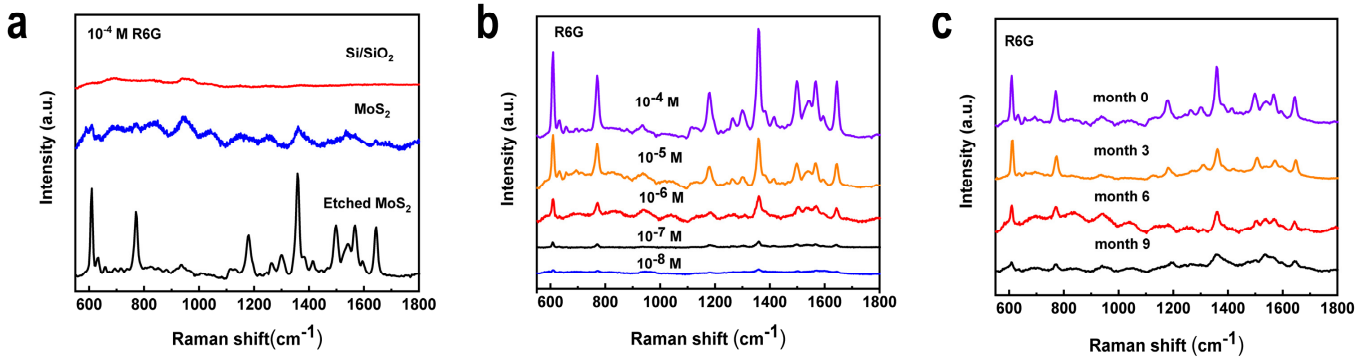

Figure 3. SERS measurements of rhodamine 6G (R6G) molecular probes on the etched monolayer MoS_2 substrates: (**a**) Raman peaks of 10^{-4} M R6G; (**b**) Concentration-dependent SERS spectra from 10^{-8} M to 10^{-4} M; (**c**) The stability ratio of 10^{-5} M R6G coated on the etched MoS_2.

To further explore the wide applications of defect-containing MoS_2 for SERS, tests were performed with different concentrations of CV and MB molecules under the same test conditions. The Raman peaks of methylene blue (MB) molecules located at 1625 and 1398 cm^{-1}, and crystal violet (CV) molecules located at wavenumbers of 918, 1177, 1376, 1587, and 1620 cm^{-1} were detected (Figure S11) [17]. The LODs of both molecules can reach 10^{-8} M, which is superior to most semiconductor SERS substrates. The monolayer MoS_2 grown on the same SiO_2/Si exhibited a high onset of SERS signal measured after the etching reaction. When CV was the detection molecule (Figure S12), the relative standard deviations (RSD) of Raman peaks at 1620 cm^{-1} were calculated to be 6.2%. This result is due to the homogeneity of the defect generation process by etching and, to a lesser extent, the relatively strong and homogeneous interaction between the dye molecule and the etched MoS_2 surface. The stability of SERS measurements is also a key issue for application. Etched MoS_2 samples with deposited R6G (10^{-5} M) were exposed to a typical laboratory temperature atmosphere for 9 months for in situ Raman measurements (Figure 3c). The results show that the Raman intensity of the characteristic R6G (10^{-5} M) peak at 1640 cm^{-1} on the substrate still maintains 20% SERS activity after 9 months (Figure S13). This period is rare among the reported SERS substrates and confirms the excellent stability of the etched substrate under air exposure [9]. The excellent detection performance of etched monolayer MoS_2 contributes to the establishment of a general method for the application of a wide range of semiconductor SERS sensors in realistic analytical scenarios.

To further clarify the enhancement mechanism in-depth for the excellent SERS activity of 2D etched monolayer MoS_2, systematic investigations have been conducted by theory simulations. DOS simulations further show that the Fermi energy level of the etched monolayer MoS_2 is elevated due to the presence of surface defects. Relatively, the free electron and charge densities of etched MoS_2 near the Fermi energy level are increased. These changes are expected to have important implications for SERS performance due to increased PICT jumps as well as substrate-molecule interactions. The highest occupied molecular orbital (HOMO) and lowest-unoccupied molecular orbital (LUMO) levels of R6G were −3.46 eV and −6.28 eV, respectively (Figure 4b).

Based on the above experimental results and theoretical analysis, possible charge transfer mechanisms of multiple dye molecules were further considered to better understand the differences between monolayer MoS_2 and defect-containing monolayer MoS_2. Monolayer MoS_2 absorbs more dye molecules after etching than before etching, but this is not enough to greatly enhance the SERS performance. The electron transfer of monolayer MoS_2 under laser irradiation at 532 nm (2.33 eV) can be described by a two-step process. Process I is a molecular leap (μ_{mol}), in which electrons are excited at the HOMO energy level to the LUMO energy level of R6G, leaving holes in the HOMO. Process II, the PICT leap process (μ_{PICT}) based on the CM mechanism, occurs between the substrate and the R6G molecule at the energy of the applied laser, which involves two processes: from the valence band (VB) of the monolayer MoS_2 to the HOMO of R6G, and from the HOMO

of R6G to the conduction band (CB) of the monolayer MoS_2. The process energies of these two PICT jumps are 0.65 eV and 1.01 eV, which are far below the laser light energy of 2.33 eV. In the R6G/etched MoS_2 system, in addition to the two PICT processes of VB-LUMO and HOMO-CB between R6G and the monolayer MoS_2, there is also a coupling of etched MoS_2 to R6G. The CB and VB of etched MoS_2 are located at −3.79 eV and −3.86 eV, respectively (Figure S14). The PICT jumps from the R6G HOMO to the etched MoS_2 Fermi energy level and then from the etched MoS_2 Fermi energy level to the LUMO of R6G, which in turn generates a wide range of charge transfer resonance energies. The resonance gains intensity from the molecular leap through vibrational coupling, which greatly amplifies the polarization tensor of the probe. In general, the polarization tensor is expressed as $\alpha = A + B + C$, where A is associated with the molecular resonance and B and C represent the two charge-transfer resonances [46]. In addition to the charge transfer resonance, molecular resonance at 532 nm excitation also increases the cross-section of the Raman scattering probe, whereas no detectable SERS signal is collected at the 633 nm laser wavelength (Figure S15) [47]. Second, molecular fluorescence background burst is also considered as another manifestation of charge transfer in the R6G/etched MoS_2 system. Based on the above points, defect-containing MoS_2 exhibits stronger SERS activity than monolayer MoS_2.

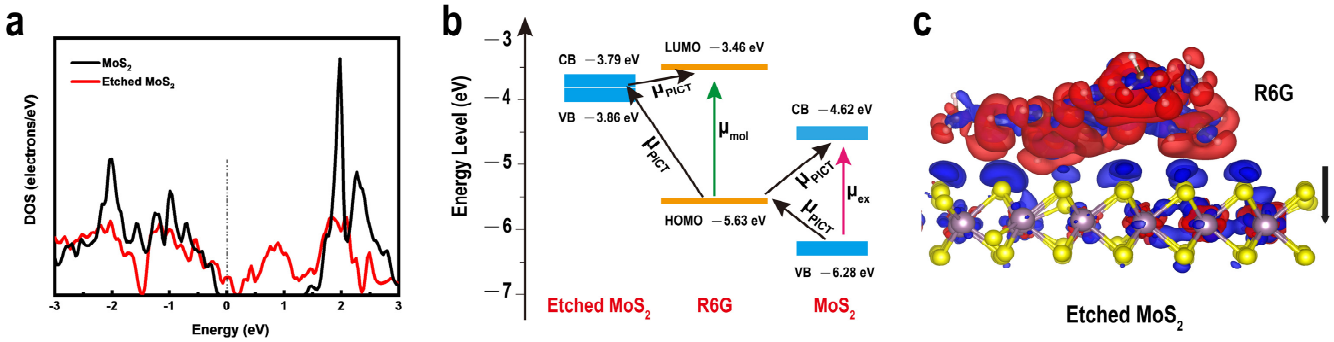

Figure 4. (**a**) Density of states of CVD grown MoS_2 and etched monolayer MoS_2. (**b**) Energy level diagram and charge transfer transitions in the diagram comparing the charge-transfer pathways in R6G/MoS_2 and R6G/etched MoS_2-MoS_2. (**c**) Side views of the electron density difference isosurface for the R6G molecule absorbed on etched monolayer MoS_2.

The CV and MB molecules on the MoS_2 substrate with defects also greatly enhance the SERS performance due to the CM-based PICT leap (Figure S14) due to the stability (a) and its ratio (b) of 10^{-5} M R6G coated on the etched MoS_2. The electron transfer process between CV and MB molecules and MoS_2 is much more complicated. In addition to their μ_{ex}, two PICT processes, VB-LUMO and HOMO-CB, occur between the two molecules and the unetched MoS_2, as shown in Figure S14. In CV/etched MoS_2 or MB/etched MoS_2, the charge of the LUMO of CV or MB must jump further to the Fermi energy level of the etched MoS_2. This process is advantageous, and metallic defect-containing MoS_2 with abundant DOS near the Fermi energy level as well as strong interactions with analytes also enhance SERS properties. The known μ_{mol} energies are 1.79 eV and 1.80 eV for CV and MB molecules, respectively. These values are less than 2.17 eV, which is the μ_{mol} energy for R6G molecules. At the same excitation energy, the SERS performance of CV and MB molecules is nevertheless consistent with that of R6G, which may be caused by the weakening of the resonance energy between the substrate and the molecule.

The coupling and PICT modes between the three dye molecules and the etched MoS_2 were investigated using density flooding theory. Side views of the electron density difference equivalence surface were used to interpret the CT direction more intuitively (Figures 4c and S16). The blue area is used to indicate an increase in the charge density, and the red area is used to indicate a decrease in charge density. There is a general loss of electrons on the dye molecule and an overall electron-rich state in the MoS_2. The electrons

and holes generated by charge transfer are closely located around the defective MoS_2 surface and the dye molecules, forming dipoles at the interface, and the dipole resonance excites the SERS effect of the dyes on the etched MoS_2. Additionally, the presence of regions of increased and decreased electron density on both R6G, MB, and CV and monolayer MoS_2 containing defects indicates that the charge transfer in the energy band structure is reasonable and that this defect preparation strategy is effective for the enhancement of the SERS performance of monolayer MoS_2.

4. Conclusions

In summary, a strategy to prepare defects by etching was applied to monolayer MoS_2. Defects are considered to be the absence of Mo and S atoms, which leads to changes in the MoS_2 surface and energy band structure. The defects tend to be in a metallic state. This change results in a dramatic improvement in the SERS properties of monolayer MoS_2. Substrates prepared from defect-containing monolayer MoS_2 can not only detect a wide range of dye molecules but also maintain ultrahigh reproducibility and stability. The results of theoretical calculations show that the static coupling between the dye molecules and the monolayer MoS_2 containing defects, the increase in the DOS near the Fermi level, and the enhancement of the charge transfer resonance make SERS detection more sensitive. Etched MoS_2 is a new strategy for the molecular engineering of 2D materials and provides new ideas for SERS applications of other TMDCS materials, making it promising for both materials science and chemistry.

Supplementary Materials: The following supporting information can be downloaded at: https://www.mdpi.com/article/10.3390/nano12060896/s1, Figure S1: (a,b) SEM image of the untreated and electroplated surface of Mo foil; Figure S2: Schematic illustration of CVD system growing monolayer MoS_2; Figure S3: Schematic illustration of the etching process of monolayer MoS_2; Figure S4: AFM image of (a) monolayer MoS_2, (b) mild etching monolayer MoS_2, (c) moderate etching monolayer of MoS_2, (d) severe etching monolayer of MoS_2; Figure S5: 3D AFM image of (a) monolayer MoS_2 and (b) moderate etching monolayer MoS_2; Figure S6: Optical photograph of dye molecules added dropwise on unetched monolayer MoS_2; Figure S7: PL spectra of monolayer MoS_2 and etched monolayer MoS_2; Figure S8: The calculated band structures of MoS_2 take Fermi level as reference; Figure S9: O 1s XPS spectrum of commercial MoS_2 powder, CVD grown monolayer MoS_2, and etched monolayer MoS_2; Figure S10: The enhancement factor (EF) of etched MoS_2 overlay 10^{-4} M R6G; Figure S11: SERS measurements of crystal violet (CV), and methylene blue (MB) molecules probes on etched monolayer MoS_2 substrates; Figure S12: (a) SERS spectra of CV (10^{-5} M) coated on etched MoS_2 taken from 15 randomly chosen spots. (b) Histogram distribution of the Raman intensities at 1620 cm^{-1}; Figure S13: The stability ratio of 10^{-5} M R6G coated on etched MoS_2; Figure S14: Energy level diagram and charge transfer transitions in the diagram comparing the charge-transfer pathways in CV/etched MoS_2 and MB/etched MoS_2; Figure S15:The Raman signals of 10^{-5} M R6G coated on etched MoS_2 were irradiated at 532 nm and 633 nm, respectively; Figure S16: Side views of the electron density difference isosurface for MB (a), and CV (b) molecule absorbed on etched monolayer MoS_2.

Author Contributions: Conceptualization, G.X. and X.L.; methodology, S.S., J.Z., R.S. and D.W.; software, G.X., S.S.; validation, J.Z., X.L. and X.Z.; formal analysis, X.L., J.Z. and G.X.; investigation, S.S., R.S.; resources, H.G., Y.L. and D.L.; data curation, G.S., Y.L.; writing—original draft preparation, S.S., J.Z., G.X. and X.L.; writing—review and editing, S.S., J.Z., G.X. and X.L.; visualization, S.S.; supervision, X.Z., H.G.; project administration, Y.L., D.L. and M.G.; funding acquisition, G.X., X.Z., X.L. and M.G. All authors have read and agreed to the published version of the manuscript.

Funding: This work was funded by the National Natural Science Foundation of China (61903235, 51808328 and 22005160) and the Major Scientific and Technological Innovation Project of Shandong (2020CXGC010309).

Institutional Review Board Statement: Not applicable.

Informed Consent Statement: Not applicable.

Data Availability Statement: Data are available on the request of the corresponding author.

Conflicts of Interest: The authors declare no conflict of interest.

References

1. Wang, Y.; Iglesias, D.; Gali, S.M.; Beljonne, D.; Samorì, P. Light-Programmable Logic-in-Memory in 2D Semiconductors Enabled by Supramolecular Functionalization: Photoresponsive Collective Effect of Aligned Molecular Dipoles. *ACS Nano* **2021**, *15*, 13732–13741. [CrossRef] [PubMed]
2. Wang, Y.; Gali, S.M.; Slassi, A.; Beljonne, D.; Samorì, P. Collective Dipole-Dominated Doping of Monolayer MoS_2: Orientation and Magnitude Control via the Supramolecular Approach. *Adv. Funct. Mater.* **2020**, *30*, 2002846. [CrossRef]
3. Qiu, H.; Liu, Z.; Yao, Y.; Herder, M.; Hecht, S.; Samorì, P. Simultaneous Optical Tuning of Hole and Electron Transport in Ambipolar WSe_2 Interfaced with a Bicomponent Photochromic Layer: From High-Mobility Transistors to Flexible Multilevel Memories. *Adv. Mater.* **2020**, *32*, 1907903. [CrossRef]
4. Calavalle, F.; Dreher, P.; Surdendran, A.P.; Wan, W.; Timpel, M.; Verucchi, R.; Rogero, C.; Bauch, T.; Lombardi, F.; Casanova, F.; et al. Tailoring Superconductivity in Large-Area Single-Layer $NbSe_2$ via Self-Assembled Molecular Adlayers. *Nano Lett.* **2021**, *21*, 136–143. [CrossRef] [PubMed]
5. Xu, G.; Wang, X.; Sun, Y.; Chen, X.; Zheng, J.; Sun, L.; Jiao, L.; Li, J. Metallic and ferromagnetic MoS_2 nanobelts with vertically aligned edges. *Nano Res.* **2015**, *8*, 2946–2953. [CrossRef]
6. Chen, M.; Liu, D.; Du, X.; Lo, K.H.; Wang, S.; Zhou, B.; Pan, H. 2D materials: Excellent substrates for surface-enhanced Raman scattering (SERS) in chemical sensing and biosensing. *Trends Anal. Chem.* **2020**, *130*, 115983. [CrossRef]
7. Nie, S.; Emory, S.R. Probing Single Molecules and Single Nanoparticles by Surface-Enhanced Raman Scattering. *Science* **1997**, *275*, 1102–1106. [CrossRef]
8. Schlücker, S. Surface-Enhanced Raman Spectroscopy: Concepts and Chemical Applications. *Angew. Chem. Int. Ed.* **2014**, *53*, 4756–4795. [CrossRef]
9. Tao, L.; Chen, K.; Chen, Z.; Cong, C.; Qiu, C.; Chen, J.; Wang, X.; Chen, H.; Yu, T.; Xie, W.; et al. 1T′ Transition Metal Telluride Atomic Layers for Plasmon-Free SERS at Femtomolar Levels. *J. Am. Chem. Soc.* **2018**, *140*, 8696–8704. [CrossRef]
10. Langer, J.; de Aberasturi, D.J.; Aizpurua, J.; Alvarez-Puebla, R.A.; Auguié, B.; Baumberg, J.J.; Bazan, G.C.; Bell, S.E.J.; Boisen, A.; Brolo, A.G.; et al. Present and Future of Surface-Enhanced Raman Scattering. *ACS Nano* **2020**, *14*, 28–117. [CrossRef]
11. Liu, R.; Jiang, L.; Yu, Z.; Jing, X.; Liang, X.; Wang, D.; Yang, B.; Lu, C.; Zhou, W.; Jin, S. MXene ($Ti_3C_2T_x$)-Ag nanocomplex as efficient and quantitative SERS biosensor platform by in-situ PDDA electrostatic self-assembly synthesis strategy. *Sens. Actuators B Chem.* **2021**, *333*, 129581. [CrossRef]
12. Yu, J.; Yang, M.; Li, Z.; Liu, C.; Wei, Y.; Zhang, C.; Man, B.; Lei, F. Hierarchical Particle-In-Quasicavity Architecture for Ultratrace In Situ Raman Sensing and Its Application in Real-Time Monitoring of Toxic Pollutants. *Anal. Chem.* **2020**, *92*, 14754–14761. [CrossRef] [PubMed]
13. Song, X.; Yi, W.; Li, J.; Kong, Q.; Bai, H.; Xi, G. Selective Preparation of Mo_2N and MoN with High Surface Area for Flexible SERS Sensing. *Nano Lett.* **2021**, *21*, 4410–4414. [CrossRef] [PubMed]
14. Bell, S.E.J.; Charron, G.; Cortés, E.; Kneipp, J.; de la Chapelle, M.L.; Langer, J.; Procházka, M.; Tran, V.; Schlücker, S. Towards Reliable and Quantitative Surface-Enhanced Raman Scattering (SERS): From Key Parameters to Good Analytical Practice. *Angew. Chem. Int. Ed.* **2020**, *59*, 5454–5462. [CrossRef]
15. Liang, X.; Li, N.; Zhang, R.; Yin, P.; Zhang, C.; Yang, N.; Liang, K.; Kong, B. Carbon-based SERS biosensor: From substrate design to sensing and bioapplication. *NPG Asia Mater.* **2021**, *13*, 8. [CrossRef]
16. Zhao, X.; Liu, C.; Yu, J.; Li, Z.; Liu, L.; Li, C.; Xu, S.; Li, W.; Man, B.; Zhang, C. Hydrophobic multiscale cavities for high-performance and self-cleaning surface-enhanced Raman spectroscopy (SERS) sensing. *Nanophotonics* **2020**, *9*, 4761–4773. [CrossRef]
17. Song, G.; Gong, W.; Cong, S.; Zhao, Z. Ultrathin Two-Dimensional Nanostructures: Surface Defects for Morphology-Driven Enhanced Semiconductor SERS. *Angew. Chem. Int. Ed.* **2021**, *60*, 5505–5511. [CrossRef]
18. Wang, X.; Shi, W.; Jin, Z.; Huang, W.; Lin, J.; Ma, G.; Li, S.; Guo, L. Remarkable SERS Activity Observed from Amorphous ZnO Nanocages. *Angew. Chem. Int. Ed.* **2017**, *56*, 9851–9855. [CrossRef]
19. Rani, R.; Yoshimura, A.; Das, S.; Sahoo, M.R.; Kundu, A.; Sahu, K.K.; Meunier, V.; Nayak, S.K.; Koratkar, N.; Hazra, K.S. Sculpting Artificial Edges in Monolayer MoS_2 for Controlled Formation of Surface-Enhanced Raman Hotspots. *ACS Nano* **2020**, *14*, 6258–6268. [CrossRef]
20. Chen, L.-Y.; Yu, J.-S.; Fujita, T.; Chen, M.-W. Nanoporous Copper with Tunable Nanoporosity for SERS Applications. *Adv. Funct. Mater.* **2009**, *19*, 1221–1226. [CrossRef]
21. Si, S.; Liang, W.; Sun, Y.; Huang, J.; Ma, W.; Liang, Z.; Bao, Q.; Jiang, L. Facile Fabrication of High-Density Sub-1-nm Gaps from Au Nanoparticle Monolayers as Reproducible SERS Substrates. *Adv. Funct. Mater.* **2016**, *26*, 8137–8145. [CrossRef]
22. Huo, D.; Chen, B.; Meng, G.; Huang, Z.; Li, M.; Lei, Y. Ag-Nanoparticles@Bacterial Nanocellulose as a 3D Flexible and Robust Surface-Enhanced Raman Scattering Substrate. *ACS Appl. Mater. Interfaces* **2020**, *12*, 50713–50720. [CrossRef] [PubMed]
23. Sun, G.; Li, N.; Wang, D.; Xu, G.; Zhang, X.; Gong, H.; Li, D.; Li, Y.; Pang, H.; Gao, M.; et al. A Novel 3D Hierarchical Plasmonic Functional $Cu@Co_3O_4@Ag$ Array as Intelligent SERS Sensing Platform with Trace Droplet Rapid Detection Ability for Pesticide Residue Detection on Fruits and Vegetables. *Nanomaterials* **2021**, *11*, 3460. [CrossRef] [PubMed]
24. Zhang, C.; Li, C.; Yu, J.; Jiang, S.; Xu, S.; Yang, C.; Liu, Y.J.; Gao, X.; Liu, A.; Man, B. SERS activated platform with three-dimensional hot spots and tunable nanometer gap. *Sens. Actuators B Chem.* **2018**, *258*, 163–171. [CrossRef]

25. Brill, A.R.; Biswas, S.; Caspary Toroker, M.; de Ruiter, G.; Koren, E. Dipole-Induced Raman Enhancement Using Noncovalent Azobenzene-Functionalized Self-Assembled Monolayers on Graphene Terraces. *ACS Appl. Mater. Interfaces* **2021**, *13*, 10271–10278. [CrossRef]
26. Gong, H.; Zheng, X.; Zeng, K.; Yang, B.; Liang, X.; Li, L.; Tao, Y.; Yang, R. Ni_3Fe nanoalloys embedded in N-doped carbon derived from dual-metal ZIF: Efficient bifunctional electrocatalyst for Zn-air battery. *Carbon* **2021**, *174*, 475–483. [CrossRef]
27. Ling, X.; Fang, W.; Lee, Y.-H.; Araujo, P.T.; Zhang, X.; Rodriguez-Nieva, J.F.; Lin, Y.; Zhang, J.; Kong, J.; Dresselhaus, M.S. Raman Enhancement Effect on Two-Dimensional Layered Materials: Graphene, h-BN and MoS_2. *Nano Lett.* **2014**, *14*, 3033–3040. [CrossRef]
28. Zhao, S.; Wang, H.; Niu, L.; Xiong, W.; Chen, Y.; Zeng, M.; Yuan, S.; Fu, L. 2D GaN for Highly Reproducible Surface Enhanced Raman Scattering. *Small* **2021**, *17*, 2103442. [CrossRef]
29. Muehlethaler, C.; Considine, C.R.; Menon, V.; Lin, W.C.; Lee, Y.H.; Lombardi, J.R.J.A.P. Ultrahigh Raman Enhancement on Monolayer MoS_2. *ACS Photonics* **2016**, *3*, 1164–1169. [CrossRef]
30. Cong, S.; Yuan, Y.; Chen, Z.; Hou, J.; Yang, M.; Su, Y.; Zhang, Y.; Li, L.; Li, Q.; Geng, F.; et al. Noble metal-comparable SERS enhancement from semiconducting metal oxides by making oxygen vacancies. *Nat. Commun.* **2015**, *6*, 7800. [CrossRef]
31. Lombardi, J.R.; Birke, R.L. Theory of Surface-Enhanced Raman Scattering in Semiconductors. *J. Phys. Chem. C* **2014**, *118*, 11120–11130. [CrossRef]
32. Zheng, Z.; Cong, S.; Gong, W.; Xuan, J.; Li, G.; Lu, W.; Geng, F.; Zhao, Z. Semiconductor SERS enhancement enabled by oxygen incorporation. *Nat. Commun.* **2017**, *8*, 1993. [CrossRef]
33. Li, Y.; Wang, D.; Xu, G.; Qiao, L.; Li, Y.; Gong, H.; Shi, L.; Li, D.; Gao, M.; Liu, G.; et al. ZIF-8/PI Nanofibrous Membranes With High-Temperature Resistance for Highly Efficient $PM_{0.3}$ Air Filtration and Oil-Water Separation. *Front. Chem.* **2021**, *9*, 810861. [CrossRef] [PubMed]
34. Wang, X.; Shi, W.; Wang, S.; Zhao, H.; Lin, J.; Yang, Z.; Chen, M.; Guo, L. Two-Dimensional Amorphous TiO_2 Nanosheets Enabling High-Efficiency Photoinduced Charge Transfer for Excellent SERS Activity. *J. Am. Chem. Soc.* **2019**, *141*, 5856–5862. [CrossRef] [PubMed]
35. Yin, Y.; Miao, P.; Zhang, Y.; Han, J.; Zhang, X.; Gong, Y.; Gu, L.; Xu, C.; Yao, T.; Xu, P.; et al. Significantly Increased Raman Enhancement on MoX_2 (X = S, Se) Monolayers upon Phase Transition. *Adv. Funct. Mater.* **2017**, *27*, 1606694. [CrossRef]
36. Sun, L.; Hu, H.; Zhan, D.; Yan, J.; Liu, L.; Teguh, J.S.; Yeow, E.K.L.; Lee, P.S.; Shen, Z. Plasma Modified MoS_2 Nanoflakes for Surface Enhanced Raman Scattering. *Small* **2014**, *10*, 1090–1095. [CrossRef]
37. Qiu, H.; Li, Z.; Gao, S.; Chen, P.; Li, H.J.R.A. Large-Area MoS_2 Thin layers Directly Synthesized on Pyramid-Si Substrate for Surface-Enhanced Raman Scattering. *RSC Adv.* **2015**, *5*, 83899–83905. [CrossRef]
38. Ippolito, S.; Kelly, A.G.; Furlan de Oliveira, R.; Stoeckel, M.-A.; Iglesias, D.; Roy, A.; Downing, C.; Bian, Z.; Lombardi, L.; Samad, Y.A.; et al. Covalently interconnected transition metal dichalcogenide networks via defect engineering for high-performance electronic devices. *Nat. Nanotechnol.* **2021**, *16*, 592–598. [CrossRef]
39. Wang, S.; Lee, G.-D.; Lee, S.; Yoon, E.; Warner, J.H. Detailed Atomic Reconstruction of Extended Line Defects in Monolayer MoS_2. *ACS Nano* **2016**, *10*, 5419–5430. [CrossRef]
40. Zheng, J.; Du, H.; Jiang, F.; Zhang, Z.; Sa, B.; He, W.; Jiao, L.; Zhan, H. Rapid and Large-Scale Quality Assessment of Two-Dimensional MoS_2 Using Sulfur Particles with Optical Visualization. *Nano Lett.* **2021**, *21*, 1260–1266. [CrossRef]
41. Zheng, J.; Yan, X.; Lu, Z.; Qiu, H.; Xu, G.; Zhou, X.; Wang, P.; Pan, X.; Liu, K.; Jiao, L. High-Mobility Multilayered MoS_2 Flakes with Low Contact Resistance Grown by Chemical Vapor Deposition. *Adv. Mater.* **2017**, *29*, 1604540. [CrossRef] [PubMed]
42. Sun, R.; Sun, S.; Liang, X.; Gong, H.; Zhang, X.; Li, Y.; Gao, M.; Li, D.; Xu, G. Surface Charge Transfer Doping of MoS_2 Monolayer by Molecules with Aggregation-Induced Emission Effect. *Nanomaterials* **2022**, *12*, 164. [CrossRef] [PubMed]
43. Kresse, G.; Joubert, D. From ultrasoft pseudopotentials to the projector augmented-wave method. *Phys. Rev. B* **1999**, *59*, 1758–1775. [CrossRef]
44. Perdew, J.P.; Burke, K.; Ernzerhof, M. Generalized Gradient Approximation Made Simple. *Phys. Rev. Lett.* **1996**, *77*, 3865–3868. [CrossRef] [PubMed]
45. Sun, L.; Yan, X.; Zheng, J.; Yu, H.; Lu, Z.; Gao, S.-p.; Liu, L.; Pan, X.; Wang, D.; Wang, Z.; et al. Layer-Dependent Chemically Induced Phase Transition of Two-Dimensional MoS_2. *Nano Lett.* **2018**, *18*, 3435–3440. [CrossRef] [PubMed]
46. Lombardi, J.R.; Birke, R.L. A Unified Approach to Surface-Enhanced Raman Spectroscopy. *J. Phys. Chem. C* **2008**, *112*, 5605–5617. [CrossRef]
47. Jensen, L.; Schatz, G.C. Resonance Raman Scattering of Rhodamine 6G as Calculated Using Time-Dependent Density Functional Theory. *J. Phys. Chem. A* **2006**, *110*, 5973–5977. [CrossRef]